


 Cite this: *Phys. Chem. Chem. Phys.*,
2026, 28, 11161

Designing multi-site charge-bifurcation networks in *de novo* proteins: a kinetic, statistical, and machine-learning approach

 Xiao Huang,^a William F. DeGrado,^b Michael J. Therien^a and David N. Beratan^{c,d}

Electron bifurcation reactions separate electron pairs into high and low potential pools, and these reactions are central to the bioenergetics of living systems. Here, we used kinetic analysis and machine learning to analyze a diverse set of structural and electrochemical landscapes that may guide the design of molecular architectures that could serve as experimental targets that would function to bifurcate holes using light. We find that strong electrostatic repulsion between the holes enhances the quantum yield for bifurcation but reduces the energy efficiency of the process. We find that the quantum yield for hole bifurcation is enhanced by positioning the hot-hole pathway cofactor farther from the hole bifurcation site than its cold-hole pathway counterpart. This integrated design and optimization approach provides design strategies for *de novo* structures that could realize light-drive hole bifurcation, advancing the aim of employing bioinspired electron bifurcation for energy conversion, photocatalysis, and electrocatalysis. Beyond the specific light-driven hole-bifurcation architecture, our combined kinetic–statistical–machine-learning approach is transferable to other multi-particle, multi-site charge-transport network design challenges, opening paths for designing photochemical and catalytic networks, as well as for designing functional redox networks.

 Received 9th February 2026,
Accepted 27th March 2026

DOI: 10.1039/d6cp00473c

rsc.li/pccp

1 Introduction

Electron bifurcation (EB) reactions are poorly understood but central in bioenergetics, splitting electron pairs on a donor cofactor into two spatially separated pools at very different electrochemical potentials.^{1,2} EB reactions occur in photosynthesis, respiration, and biocatalysis, underpinning nitrogen fixation, carbon dioxide reduction, and hydrogen production. Cytochrome *bc*₁, cytochrome *b*_{6f}, and certain flavoproteins perform electron bifurcation reactions.^{1,3,4}

Realizing electron or hole bifurcation in a *de novo* protein framework^{5–8} represents an unrealized challenge, although some basic design principles are emerging.^{9,10} EB delivers electrons into redox pools at different potentials and, as such, is an open-system reaction. A challenge faced by the EB networks is to avoid electron leakage (or short circuiting) between the low and high potential pathways. Short circuiting avoidance

makes the design and synthesis of electron bifurcating networks very challenging.^{3,4,9,11} In our earlier analysis of light-driven hole bifurcation (HB),¹⁰ we described architectures (with specific electrochemical gradients and inter-cofactor distances) that could support light-driven HB. Our earlier photoinduced HB design relied on having two nearby tryptophan residues that are oxidized sequentially by photoactivated (ruthenium) chromophores bound to the *de novo* protein's surface. Rapid sequential Trp oxidation would produce electrostatic repulsion between two nearby radical cation states, energizing the system. As each hole migrates along a spatially separated pathway, the first and second holes would depart the bifurcation site at two different potentials. The first hole to depart is expected to be more strongly oxidizing, or “hot” due to hole–hole repulsion, while the second hole to leave will be less oxidizing, or “cold”. These holes are directed onto spatially separated transport pathways that lead to terminal sites where they could carry out further redox chemistry. The design is shown schematically in Fig. 1 and 2.

Earlier kinetic analysis found that the distances and electrochemical potentials of the cofactors determine the quantum yields for delivering the holes to the chain termini. Even small changes to hopping site distances or electrochemical potentials can dramatically alter the network's bifurcation efficiency.

^a Department of Chemistry, Duke University, Durham, NC 27708, USA.

E-mail: david.beratan@duke.edu

^b Department of Pharmaceutical Chemistry, University of California, San Francisco, San Francisco, CA 94143, USA

^c Department of Biochemistry, Duke University, Durham, NC 27710, USA

^d Department of Physics, Duke University, Durham, NC 27708, USA

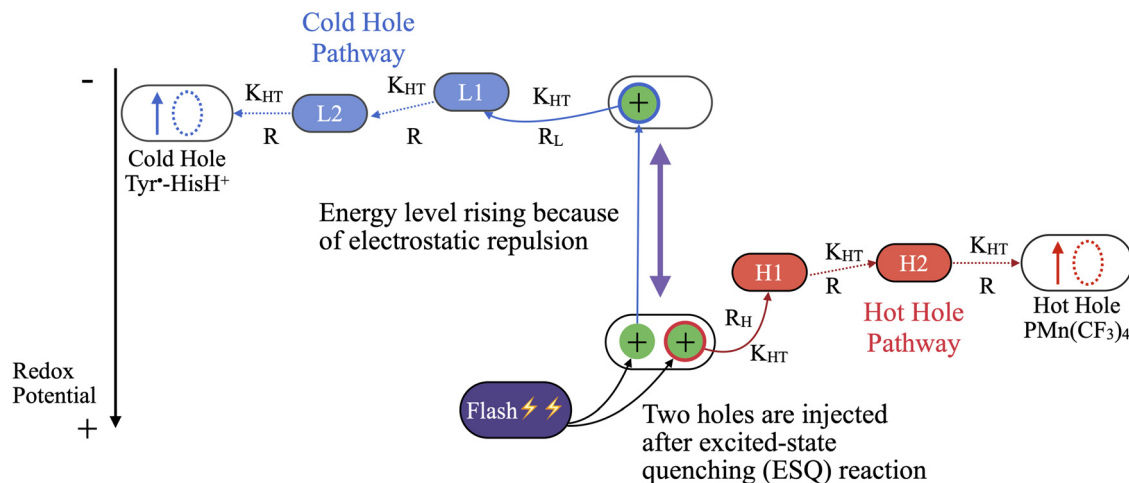



Fig. 1 Schematic representation of a light-driven *de novo* hole bifurcating system. Two flashes, in rapid succession, oxidize nearby Trp residues using photo-generated Ru(III) species attached to the protein (via a flash-quench scheme).¹⁴ The photogenerated holes hop on “hot” and “cold” hole transport pathways. The holes arrive at the termini of the pathways. The redox cycle is completed when the initial electron quencher re-reduces these terminal species.¹⁴ This figure is reproduced from ref. 10, available under a CC-BY 4.0 license, and is copyrighted by X. Huang, P. Zhang, J. L. Yuly, W. F. DeGrado, M. J. Therien, and D. N. Beratan.

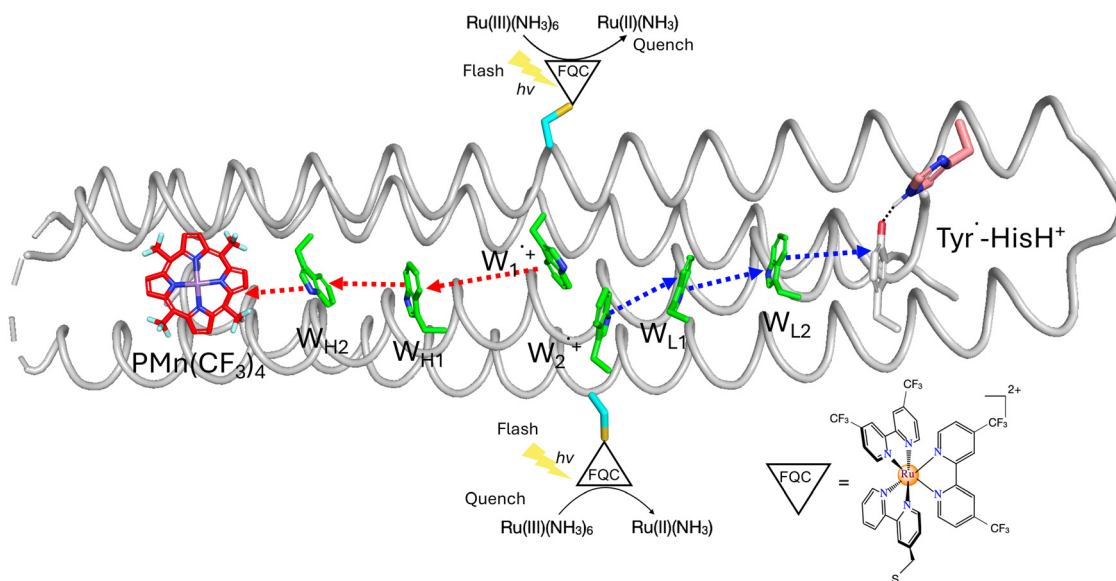


Fig. 2 An illustrative molecular model of a designed *de novo* hole bifurcating protein. Two ruthenium flash-quench chromophores (FQC) are covalently bound on the protein surface nearby two Trp (W_1 and W_2) residues. Following W_1 and W_2 photooxidation, hole transfer proceeds along two spatially separated pathways: the hot-hole path ($W_1 \rightarrow W_{H1} \rightarrow W_{H2} \rightarrow \text{PMn}(\text{CF}_3)_4$, shown in the red-arrow pathway) and the cold-hole path ($W_2 \rightarrow W_{L1} \rightarrow W_{L2} \rightarrow \text{Tyr}^{\cdot-}\text{-HisH}^+$, in the blue-arrow pathway). The two hole transfer routes terminate on acceptors tuned to different reduction potentials. This design demonstrates how light can initiate bifurcation in a synthetic, protein-based construct. This figure is reproduced from ref. 10, available under a CC-BY 4.0 license, and is copyrighted by X. Huang, P. Zhang, J. L. Yuly, W. F. DeGrado, M. J. Therien, and D. N. Beratan.

Earlier studies of open system EB in the steady state focused on networks with uniform spacings between the nearest neighbor hopping sites, three (infinite) charge reservoirs, and equal magnitude slopes for the high- and low-electrochemical potential chains.^{9,12,13} The aim of the present study is to discover molecular designs that could produce high HB quantum yields (while maintaining acceptable energy efficiency) on closed HB networks without enforcing the simplifying

constraints used in the earlier models for open system EB. This optimization focuses on the molecular architectures illustrated in Fig. 1 and 2. That is, we aimed to optimize light driven HB in *de novo* proteins where one high potential and one low potential electron hopping pathway direct charge from the two-hole bifurcation locus.

We combined kinetic network analysis, robust statistical analyses of large hole bifurcation designs, and machine



learning models to study hole bifurcation target systems. Using Bayesian optimization of HB network quantum yield and random (unbiased) sampling of the design space, we learned how structural and energetic design parameters influence HB network quantum yields and energy efficiencies. This approach to bifurcation network design produced new insights with respect to earlier EB designs that were focused on near-reversible, open-system biological structures that operate in the steady state in contact with electron reservoirs. Our optimization of closed-system, light-driven hole bifurcation finds that high quantum yield HB can be realized with acceptable energy efficiency across a surprisingly wide range of energy and distance landscapes.

While our immediate focus is on two-hole bifurcation networks in *de novo* proteins, the challenge that we address, namely how to design functional kinetic networks assisted by machine-learning, is of broader interest. The design strategy that we describe can be mapped to other multi-site, multi-particle charge-transport or bifurcation networks in proteins, molecular materials, or supramolecular assemblies.

2 Methods

2.1 Computational methods and performance assessment for enumerated bifurcation networks

To develop HB design principles for the networks with the structure shown in Fig. 1, we developed a computational protocol to build, evaluate, and analyze a large set of (theoretical) light-driven HB networks with the architecture shown in Fig. 1.

The rate constants (k_{ij}) for non-adiabatic hole transfer (HT) between pairs of redox active cofactors i and j were calculated using non-adiabatic electron transfer theory, accounting for one high-frequency (quantum) vibrational mode, shown in eqn (1):^{15,16}

$$k_{i \rightarrow j} = \frac{2\pi \langle V_{ij}^2 \rangle}{\hbar} \frac{1}{\sqrt{4\pi\lambda_{ij}k_{\text{B}}T}} \sum_n \frac{e^{-D}}{n!} D^n \exp \left[-\frac{(\Delta G_{ij} + \lambda_{ij} + n\hbar\omega)^2}{4\lambda_{ij}k_{\text{B}}T} \right] \quad (1)$$

For a given hole transfer reaction, $\langle V_{ij}^2 \rangle$ is the thermally averaged electronic coupling; $\Delta G_{ij}^{(0)}$ is the free energy change; λ_{ij} is the outer-sphere reorganization energy; D is the Huang-Rhys factor, equal to $\lambda_{\text{in}}/(\hbar\omega)$, where λ_{in} is the reorganization energy of the high frequency mode; and $\hbar\omega$ is the energy spacing for the (harmonic) high-frequency mode (see Section S1 for the estimated values for the parameters in eqn (1) and (2)).

The mean-squared electronic coupling, $\langle V_{ij}^2 \rangle$, is typically approximated using an exponential decay model reflecting its sensitivity to the inter-cofactor distance R_{ij} ,¹⁷ shown in eqn (2)

$$V_{ij} = V_0 e^{-\beta R_{ij}} \quad (2)$$

Here, R_{ij} is the edge-to-edge distance between the donor and acceptor heavy atoms.

The occupancy status of each cofactor within the network for any given redox microstate is represented by a vector \mathbf{S} . For a

system with N cofactors, $[C_1, C_2, \dots, C_N]$, \mathbf{S} is formulated as eqn (3):

$$\mathbf{S} = [n_1, n_2, \dots, n_N] \quad (3)$$

where n_i denotes the presence (+1 \hbar) or absence (0) of a hole on cofactor i .

The time evolving hole population on the network was simulated using a kinetic master equation based on the system microstates. The probability $P(S_i, t)$ of being in microstate S_i (defined by the hole occupancy of each cofactor) at time t evolves according to eqn (4):

$$\frac{d\mathbf{P}(S_i, t)}{dt} = \sum_j (K_{ij}P(S_j, t) - K_{ji}P(S_i, t)) \quad (4)$$

where K_{ij} is the transition rate matrix element linking microstate S_j to microstate S_i , and its off-diagonal elements are the individual HT rates (k_{ij}). In this model, one-electron transitions link the system microstates. The time-dependent population of microstates is shown in eqn (5):

$$\mathbf{P}(t) = e^{\mathbf{K}t} \mathbf{P}(0) \quad (5)$$

where $\mathbf{P}(t)$ is the vector of microstate probabilities at time t , $\mathbf{P}(0)$ is the initial state probability vector (with two holes localized at the bifurcation site prior to the light flash), and \mathbf{K} is the rate matrix (see eqn (6)).

$$\mathbf{K} = \begin{bmatrix} k_{11} & k_{12} & k_{13} & \cdots \\ k_{21} & k_{22} & k_{23} & \cdots \\ k_{31} & k_{32} & k_{33} & \cdots \\ \vdots & \vdots & \vdots & \ddots \end{bmatrix} \quad (6)$$

The diagonal elements of the rate matrix, k_{ii} , are the negative sums of all rates from microstate S_i to all other microstates:

$$k_{ii} = -\sum_{j \neq i} k_{ji} \quad (7)$$

The quantum yield (QY) for HB is defined as the probability for the system to reach the final state where a hole resides on each of the two terminal acceptors for a long time ($t = 1$ s). This is calculated by summing the probabilities of all microstates S where both terminal cofactors are occupied:

$$\text{QY} = \sum_{S \in S_{\text{terminal}}} P(S, t_{\text{final}}) \quad (8)$$

where S_{terminal} represents the subset of system microstates defined by the occupancy vector $n_{\text{PMn}} = 1$ and $n_{\text{Tyr}} = 1$.

We define the energy efficiency metric, η , as in eqn (9):

$$\eta = \frac{E_{\text{PMn}}^{(0)} - E_{\text{W}_2}^{(0)}}{E_{\text{repulsion}}} \quad (9)$$

$E_{\text{PMn}}^{(0)}$ in eqn (5) is the electrochemical potential of the hot-hole acceptor, $E_{\text{W}_2}^{(0)}$ is the potential of the second tryptophan (W_2) at the bifurcation site (this potential is relevant after the first hole leaves), and $E_{\text{repulsion}}$ is the electrostatic repulsion energy between the two holes at their site formation ($\text{W}_1^{\bullet+}$ and $\text{W}_2^{\bullet+}$). In our earlier study, $E_{\text{repulsion}}$ has been shown to be as



much as 1.6 eV according to the DFT calculations, and tunable as a function of edge-to-edge distance between $W_1^{\bullet+}$ and $W_2^{\bullet+}$.¹⁰

2.2 Synthetic HB network candidate generation and network parameters space sampling

We generate a large number of candidate bifurcation networks, as described below, and then analyze their performance. Each network candidate has a bifurcation site (with two interacting tryptophan residues, W_1 and W_2) and two distinct hole transport paths—designated as the low potential (hot-hole) and high potential (cold-hole) branches. Each pathway contains two cofactors (W_{H_1} , W_{H_2} and W_{L_1} , W_{L_2} , respectively). This basic architecture is motivated by the structure of the Nfn1 bifurcating flavoprotein.¹⁸ These branches each terminate at a hole acceptor. Our earlier study used a Mn porphyrin cofactor and a Tyr-HisH⁺ species as terminal hole acceptors.¹⁰ The description of a candidate HB landscape requires the enumeration of both redox group positions (edge-to-edge distances between redox species) and the electrochemical potentials of each species. R_H and R_L are the distances between the edge of the bifurcating cofactor and the nearest high and low potential acceptor. All other nearest-neighbor edge-to-edge distances (*i.e.*, the separations between successive cofactors along both the hot- and cold-hole pathways, excluding R_H and R_L) were assigned a single, common value R . This global parameter R was then varied during the optimization to explore its impact on network performance. Electrochemical potentials ($E_i^{(0)}$) for each cofactor, reorganization energies (λ_{ij}), and the electrostatic repulsion between the two oxidized cofactors at the bifurcation site are all included in the landscape models. The midpoint potential for the terminal Tyr-His/Tyr[•]-HisH⁺ redox couple is estimated to be approximately 1.0 V (*vs.* NHE)^{19–23} and is not varied. The electrochemical potential of the terminal MnP species is varied, as this potential could be altered by changes to the chemical composition or the protein environment.

Table 1 shows the range of electron transfer rate parameters (reorganization energies, electrochemical potentials, distances) that are selected to span biologically and synthetically plausible ranges. The parameter ranges in Table 1 were selected to span

Table 1 Parameters defining the HB kinetic model. Ranges represent biologically plausible and synthetically accessible values

Parameter	Range
Reduction potential of cofactor W_2 ($E_{W_2}^{(0)}$)	0.8 eV to 1.3 eV
Electrostatic repulsion ($E_{\text{repulsion}}$)	0.5 eV to 1.8 eV
Reduction potential of cofactor W_{L_1} ($E_{W_{L_1}}^{(0)}$)	0.8 V to 1.2 V
Reduction potential of cofactor W_{H_1} ($E_{W_{H_1}}^{(0)}$)	1.35 V to 1.95 V
Reduction potential of cofactor W_{L_2} ($E_{W_{L_2}}^{(0)}$)	0.8 V to 1.2 V
Reduction potential of cofactor W_{H_2} ($E_{W_{H_2}}^{(0)}$)	1.35 V to 1.95 V
Reduction potential of PMn ($E_{\text{PMn}}^{(0)}$)	1.35 V to 1.65 V
Edge-to-edge distance (R_H)	5 Å to 15 Å
Edge-to-edge distance (R_L)	5 Å to 15 Å
Edge-to-edge path distance (R)	5 Å to 15 Å
Reorganization energy (λ)	0.8 eV to 1.0 eV

the structural and energetic space accessible to *de novo* proteins. The redox potential ranges for tryptophan and the terminal acceptors were derived from literature reports and previous experimental measurements in various protein environments. Our workflow involved: (1) defining the plausible physiological range for each parameter, (2) performing large-scale sampling of these ranges, and (3) calculating the resulting kinetic performance for each set.

We used two complementary strategies to explore the parameter ranges for HB described in Table 1. The first 100 000 parameter sets were generated through uniform random sampling across the parameter ranges indicated in Table 1. This random dataset provides unbiased sampling of the parameter space. Then, in order to improve the exposure of high quantum yield design in the dataset, we performed data augmentation by generating 30 000 more parameter sets, which have high quantum yields (>0.9) identified *via* Bayesian optimization (BOp), using quantum yield for successful HB as the objective function (see Section S2 for BOp details). We generated a total of 130 000 distinct configurations. These datasets allow us to explore crucial factors for the design of high-efficiency HB networks.

The 130 000 candidate networks represent theoretical “redox landscapes” defined by the parameters in Table 1. Each data point in the training set is a unique combination of distances and potentials, rather than a specific atomistic molecular structure. This approach allows us to discover general design principles that can subsequently be mapped onto specific amino acid sequences and residue positions.

2.3 Statistical analysis on generated HB network candidates

We performed statistical analysis on 130 000 enumerated bifurcating networks. These networks were generated as described in Section 2.2. These networks aim to provide sufficient context to establish an understanding of how to control the quantum yield and energy efficiency of HB networks. Correlations between each network’s structural and energetic parameters and its performance metrics (quantum yield and energy efficiency) were quantified using Pearson’s correlation coefficients and visualized as a heatmap—a standard approach for preliminary feature screening in multivariate studies.²⁴ This linear regression framework enabled us to determine which parameters exert statistically significant effects on quantum yield and energy efficiency, to establish whether each effect is positive or negative (*i.e.*, its sign), and to quantify the strength (effect size) of these relationships under the assumption of linear dependence (as a first-order approximation to capture the primary trends, despite the underlying nonlinearity) between inputs and outputs (see Section S3 for full regression details).

2.4 Machine learning assessment of design parameter influence on quantum yield

2.4.1 Machine learning model selection and training. The factors that control HB quantum yield interact in highly nonlinear ways. As such, we used a supervised machine learning strategy to discover high-yield designs and to assess the most



impactful design parameters. We trained an XGBoost (eXtreme Gradient Boosting) classifier²⁵—a type of gradient-boosted decision-tree ensemble method—to distinguish “high yield” networks (quantum yield > 0.9) from “low yield” ones. That is, the ML approach accomplishes robust discrimination of high-*versus* low-yield networks by sequentially fitting decision-tree “weak learners” to the residual errors—thereby capturing complex, nonlinear interactions among parameters—and quantifies each parameter’s influence by aggregating its contribution to the ensemble’s predictions (see Section S4 for the model training details of XGBoost). We selected the XGBoost method because of its superior performance in capturing complex, non-linear dependencies and feature interactions that are typical in high-dimensional redox networks. Compared to linear regression or simpler decision trees, XGBoost’s ensemble approach provides higher predictive accuracy and more robust feature importance rankings *via* SHAP analysis.

As we described in Section 2.2, we generated 130 000 HB network design candidates. We divided them with an 8 : 2 ratio for the training and testing sets. The training set input information is the set of network edge-to-edge distances, reduction potentials, reorganization energies, electrostatic repulsion energies, and the derived parameter ΔR ($\Delta R = R_H - R_L$, to show the numerical relationships between R_H and R_L).

2.4.2 Model performance evaluation. We first define the classification outcomes summarized in Table 2 to evaluate classifier performance that distinguishes high- and low-yield HB networks. Here, the reference (true) labels are determined by the computed quantum yields, and the model predictions correspond to the classifier outputs. A true positive (TP) corresponds to a network with quantum yield > 0.9 that the model correctly predicts as high yield, while a false negative (FN) is a network that the model incorrectly predicts as having a low yield. Conversely, a true negative (TN) refers to a low-yield network (≤ 0.9) that is correctly classified as such, while a false positive (FP) is a low-yield network that is misclassified as being high yield.

With these outcomes defined, we assessed classifier performance using four standard metrics: accuracy, precision, recall, and the F1-score.²⁶ Accuracy measures the overall fraction of correctly classified parameter sets, shown in eqn (10):

$$\text{Accuracy} = \frac{\text{TP} + \text{TN}}{\text{TP} + \text{TN} + \text{FP} + \text{FN}} \quad (10)$$

Precision quantifies the reliability of positive predictions, shown in eqn (11):

$$\text{Precision} = \frac{\text{TP}}{\text{TP} + \text{FP}} \quad (11)$$

Table 2 Interpretation of classification outcomes for HB network yield prediction

	Predicted high yield	Predicted low yield
True high yield (> 0.9)	True positive (TP)	False negative (FN)
True low yield (≤ 0.9)	False positive (FP)	True negative (TN)

that is, the fraction of networks predicted to be “high yield” that indeed have quantum yield > 0.9. Recall (or sensitivity) evaluates how completely the model recovers true positives, shown in eqn (12):

$$\text{Recall} = \frac{\text{TP}}{\text{TP} + \text{FN}} \quad (12)$$

corresponding to the fraction of all genuinely high-yield networks identified by the classifier. Finally, the F1-score balances precision and recall through their harmonic mean, shown in eqn (13):

$$\text{F1} = 2 \times \frac{\text{precision} \times \text{recall}}{\text{precision} + \text{recall}} \quad (13)$$

Each of these metrics captures a distinct but complementary aspect of model performance. Accuracy provides a global measure of correct classifications, precision ensures that predicted high-yield networks are trustworthy, recall guards against missing genuinely promising designs, and the F1-score balances these competing goals. Considering all four metrics together is particularly important for HB network analysis, since the parameter space is large and highly non-linear. In this context, false positives (low-yield networks incorrectly predicted as high yield) may waste experimental resources, whereas false negatives (high-yield networks overlooked by the model) risk discarding potentially valuable designs. By jointly evaluating all four metrics, we ensure that the classifier not only identifies high-yield candidates with confidence but also avoids systematically excluding viable configurations that could advance HB experimental realization.

Since this is a theoretical design study aiming to establish fundamental principles, the “true” labels for the ML model are based on the MJL kinetic model. To account for potential discrepancies with future experimental results, we focused on identifying “sweet-spot” ranges rather than single optimal points. These broad ranges suggest that high HB performance is robust to the typical fluctuations and errors inherent in biological redox parameters.

2.4.3 Interpreting the XGBoost model with SHAP to derive HB design principles. To understand why our XGBoost model reaches its decisions, we applied SHAP (SHapley Additive exPlanations) analysis to the trained XGBoost classifier and its input features.²⁷ That is, SHAP was used to compute feature attributions from the fitted XGBoost model, quantifying how each input parameter contributed to the model’s prediction of high-*versus* low-yield outcomes. SHAP assigns a Shapley value to every feature in a given HB network configuration. Here, a feature refers to one of the structural or energetic design parameters (*e.g.*, an edge-to-edge distance, a reduction potential, or the repulsion energy) that define the network landscape. Each Shapley value represents the contribution of that feature to shifting the model’s output probability toward either the “high yield” or “low yield” class. By averaging absolute Shapley values across all instances (where an instance corresponds to one complete set of HB design parameters), we obtain a robust global ranking of feature importance.



Moreover, by analyzing Shapley value distributions across the data, we identify the ranges of each design parameter that is most conducive to producing a high yield for hole bifurcation. In this way, SHAP complements traditional linear methods (*e.g.* correlation analysis or ordinary least-squares regression) by revealing both the magnitude and the direction of nonlinear effects of the design parameters on the bifurcation yield, thus offering practical guidance for designing synthetic HB networks (see Section S5 for details of the SHAP analysis).

3 Results and discussion

To elucidate critical factors that influence the yield of hole bifurcation (HB) networks, we evaluated the relationships between network parameters (Table 1) and the bifurcation yield. Statistical analysis on the dataset of bifurcation networks, combined with feature importance assessment performed with the machine learning model XGBoost classifier, provided quantitative insight into bifurcation network design (see Section 2.2).

3.1 Correlation analysis for the design parameters and the HB performance

To identify the simplest predictive relationships between network parameters and function in our HB network, we first calculated the Pearson correlation coefficients between each input parameter and the bifurcation network performance metrics: quantum yield and energy efficiency. A heatmap shows these correlations in Fig. 3. Notably, the electrostatic repulsion between the two photogenerated holes at the bifurcation site ($E_{\text{repulsion}}$) has a moderate positive correlation with quantum yield ($r = 0.42$), indicating that stronger inter-hole repulsion generally promotes more effective bifurcation. In contrast, $E_{\text{repulsion}}$ at the bifurcation site correlates strongly and negatively with η ($r = -0.66$), indicating a clear trade-off. That is, designs that maximize HB yield tend to incur a larger energetic penalty and thus operate less efficiently. This finding is parallel to recent studies of quantum yield/energy capture tradeoffs in photosynthetic reactions.²⁸

We also studied how lowered geometric symmetry between the hot- and cold-hole pathways influences quantum yield (quantified by correlations between quantum yield and the distance difference $\Delta R = R_{\text{H}} - R_{\text{L}}$, where R_{H} and R_{L} are the edge-to-edge distances from the bifurcation site to the first hot- and cold-pathway cofactors). The value of the parameter ΔR has a robust positive correlation with the quantum yield ($r = 0.46$), suggesting that a network with a hot-pathway cofactor more distant from the bifurcation site than the cold-pathway cofactor produces higher quantum efficiencies for HB reaction. Taken together, these linear correlations provide two important design insights: (1) sufficiently large electrostatic repulsion is needed to drive high yield hole bifurcation (though this comes with a trade-off, as high repulsion simultaneously lowers the energy efficiency), and (2) maintaining a larger ΔR stabilizes the preferential routing of the hot hole onto the hot-pathway (rather than short-circuiting onto the cold-pathway), thereby enhancing the overall hole bifurcation yield.

3.2 Machine learning-based feature importance for quantum yield

We trained an XGBoost classifier to distinguish between high (quantum yield > 0.9) and low (quantum yield ≤ 0.9) yielding networks to capture the complex, nonlinear effects of design parameters on the performance of the HB networks. Our input features during the training included the full set of geometric and energetic parameters for the 104 000 HB network structures in the training set (*e.g.*, inter-cofactor distances, reduction potentials, electrostatic repulsion, reorganization energy). The classifier achieved 96.2% accuracy (along with similar high score on both precision and recall) on a held-out test set (*i.e.*, the subset of data not used during model training, reserved for independent performance evaluation) (see Table 3 for result details), demonstrating that this model is adequate to predict HB network quantum yields. We then applied SHAP analysis to this model in order to quantify the individual and combined influences of each feature on the predicted quantum yield.

SHAP analysis assesses the contribution of each input parameter (*i.e.*, inter-cofactor distances, reduction potentials,

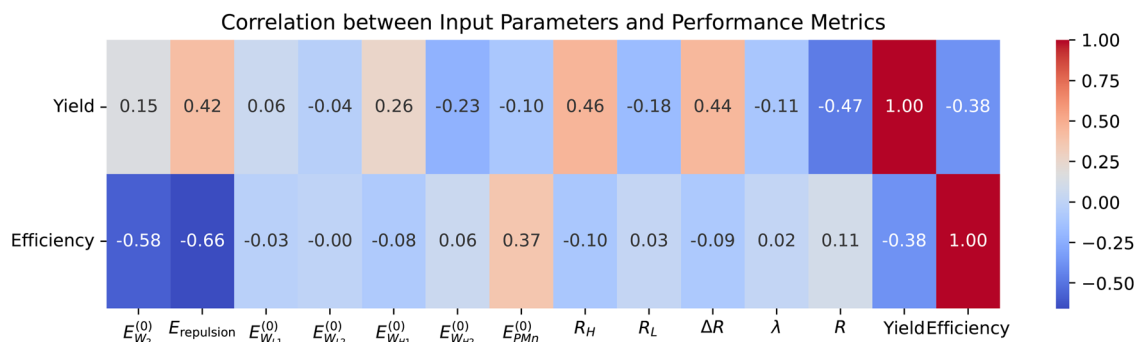


Fig. 3 Pearson correlation coefficients between input parameters (columns) and performance metrics (rows). The input parameters shown are: initial redox potentials $E_{W_2}^{(0)}$, $E_{W_{L1}}^{(0)}$, $E_{W_{L2}}^{(0)}$, $E_{W_{H1}}^{(0)}$, $E_{W_{H2}}^{(0)}$, and $E_{PMn}^{(0)}$; electrostatic repulsion energy $E_{\text{repulsion}}$; bifurcation pathway distances R_{H} and R_{L} ; the distance difference $\Delta R = R_{\text{H}} - R_{\text{L}}$; reorganization energy λ ; and inter-cofactor pathway distance R . The performance metrics shown are quantum yield (labeled yield) and energy efficiency (labeled efficiency). Red indicates positive correlation, blue indicates negative correlation, with color intensity representing the magnitude. Numerical correlation coefficients are annotated on the heatmap.



Table 3 Performance metrics for the XGBoost classifier predicting high vs. low quantum yield classes on the test set

Class	Precision	Recall	F1-score	Support
High yield (>0.9)	0.91	0.91	0.91	5520
Low yield (≤ 0.9)	0.98	0.97	0.98	20 480
Accuracy			0.96	26 000
Macro Avg.	0.94	0.94	0.94	26 000
Weighted Avg.	0.96	0.96	0.96	26 000

electrostatic repulsion, reorganization energy) to the XGBoost classifier's prediction, which distinguishes between networks yielding high (>0.9) versus low (≤ 0.9) quantum yield (Fig. 4). The summary plot in Fig. 4a shows the SHAP value for each parameter across all 130 000 generated HB network design candidate data samples. On the horizontal axis, a negative SHAP value indicates that a given parameter value shifts the model's output toward predicting a high-yield configuration, while a positive SHAP value favors a low-yield prediction. The color of each point encodes the parameter's magnitude (red = high, blue = low). For example, higher values of $E_{\text{repulsion}}$, R_{H} , and ΔR consistently produce negative SHAP values, confirming that strong hole-hole repulsion and a larger $R_{\text{H}}-R_{\text{L}}$ gap are key drivers of high quantum yield. Interestingly, larger total pathway distances R also yield negative SHAP values in this classifier—trained specifically to distinguish configurations with quantum yields above 0.9—suggesting that within the subset of already high-performing designs, shorter individual step distances can be associated with slight variations in yield that are compensated by other optimized parameters.

We ranked the network parameters by their overall influence on quantum yield, quantified as the mean absolute SHAP value across all samples, which provides a global measure of feature importance in predicting high quantum yield (Fig. 4b). In line

with the Pearson correlation results, R , $E_{\text{repulsion}}$, and R_{H} emerge as the most critical determinants of high quantum yield. This ranking informs experimental design. For example, *de novo* protein scaffolds can be engineered systematically to fine-tune these three parameters, focusing first on modulating R and R_{H} by residue positioning. Changing the amino acid composition or geometry near the bifurcation site can be used to tune $E_{\text{repulsion}}$, either by changing the local dielectric environment, introducing charged or polar residues, or altering the proximity or orientation of the bifurcating tryptophans.

When we just examine cases that produced quantum yields >0.9 , we find broad “sweet-spot” ranges for these high quantum yields (*i.e.*, yields in the 20th–80th percentile of the candidates within the high-yield subset): R between 5.4 and 8.8 Å, $E_{\text{repulsion}}$ between 1.25 and 1.71 eV, and R_{H} between 11.2 and 14.5 Å. These parameter windows, which are remarkably wide, suggest that high-performing HB networks are robust to modest changes in structure and energetics, easing the practical design of the targeted *de novo* proteins.

While the identified “sweet-spot” for $E_{\text{repulsion}}$ (1.25–1.71 eV) is high, such values are physically realizable within the specialized environments of *de novo* protein cores. The highest value of the sweet-spot has been verified in our previous work.¹⁰ By engineering the scaffold to maintain a low local dielectric constant ($\epsilon \approx 2-4$) and positioning the bifurcating tryptophans within a hydrophobic pocket shielded from the aqueous interface, the electrostatic repulsion between photogenerated radical cations can be significantly enhanced. Furthermore, our SHAP analysis indicates that the high-yield classification is robust to modest fluctuations in reorganization energy, suggesting that these designs can remain functional despite the dynamic nature of the protein matrix.

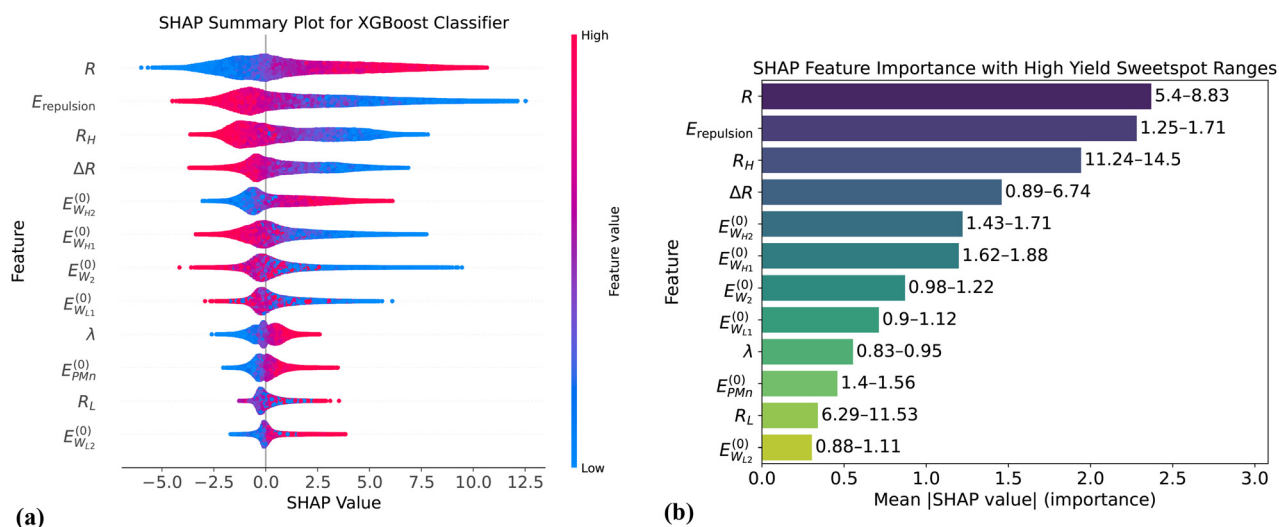


Fig. 4 SHAP analysis of the XGBoost classifier predicting high (>0.9) vs. low (≤ 0.9) quantum yield. (a) Summary plot illustrating the distribution of SHAP values for each feature. Each point represents a sample; its position on the x-axis indicates the SHAP value (impact on model output towards predicting 'low yield' if positive, 'high yield' if negative), and its color represents the feature's value for that sample (red: high, blue: low)[cite: 1]. This shows both the magnitude and direction of a feature's influence. (b) Bar plot ranking features by mean absolute SHAP value (overall importance). Text annotations indicate the “sweet spot” range (20th to 80th percentile) of feature values found in high-yield configurations.



To implement these findings, designers can tune $E_{\text{repulsion}}$ by modifying the local dielectric environment—for example, by replacing surface-exposed residues with hydrophobic ones to shield the bifurcation site. Distances like R_{H} and R can be precisely controlled by selecting specific i , $i + 7$ or i , $i + 11$ positions on an α -helix to position the cofactors. This provides a concrete roadmap for converting the identified ‘sweet spots’ into experimental protein sequences.

3.3 Visualizing performance trends for the most impactful design parameters

HB network performance depends non-linearly on the key system parameters. We performed kinetic simulations that vary individual parameters while holding others fixed to representative values (see the caption of Fig. 5 for details). Fig. 5 shows the sensitivity of the bifurcation quantum yield and energy efficiency to: (1) the distance between the bifurcation center and the hot-hole pathway (R_{H}) and (2) the electrostatic repulsion energy between the holes at the bifurcation site.

The quantum yield shows a distinctive optimal range with respect to the distance R_{H} (see Fig. 5a). Increasing R_{H} (while keeping R_{L} short) enhances the yield by directing the first (hot) hole to its high-potential pathway, consistent with the positive correlation found for quantum yield *versus* $\Delta R = R_{\text{H}} - R_{\text{L}}$. However, beyond an optimal distance (14 Å in this simulation),

the HB yield drops sharply. This decline is attributed to the exponential decay of the hole transfer rate with distance, making the second step hole transfer from W_2 to W_{L_1} too slow for productive HB. The peak performance found in this simulation aligns well with the optimal range of R_{H} values identified in the broader SHAP analysis.

The critical role of electrostatic repulsion at the bifurcating site is indicated in Fig. 5b. The quantum yield (blue curve) shows a clear threshold behavior as a function of $E_{\text{repulsion}}$, rising rapidly when the repulsion between the holes is in the ~ 0.8 – 1.1 eV window. This finding indicates that a sufficient repulsion strength is needed to provide the thermodynamic driving force required to initiate effective HB. Once hole–hole repulsion is sufficiently large (1.3 eV),¹⁰ the HB quantum yield approaches unity. The energy efficiency (orange curve) defined by eqn (9), however, shows the opposite trend. That is, the energy efficiency decreases monotonically as the hole–hole repulsion increases (that is, much of the hole–hole repulsion energy is dissipated). Fig. 5b shows key trade-offs in designing HB systems: maximizing quantum yield necessitates a high driving force to deliver the first hole, but growing the driving force for HB comes at the cost of overall energy efficiency. The repulsion energy optimal range for quantum yield identified by SHAP (1.25–1.71 eV) represents a balance among achieving a high quantum yield and an acceptable energy efficiency; near

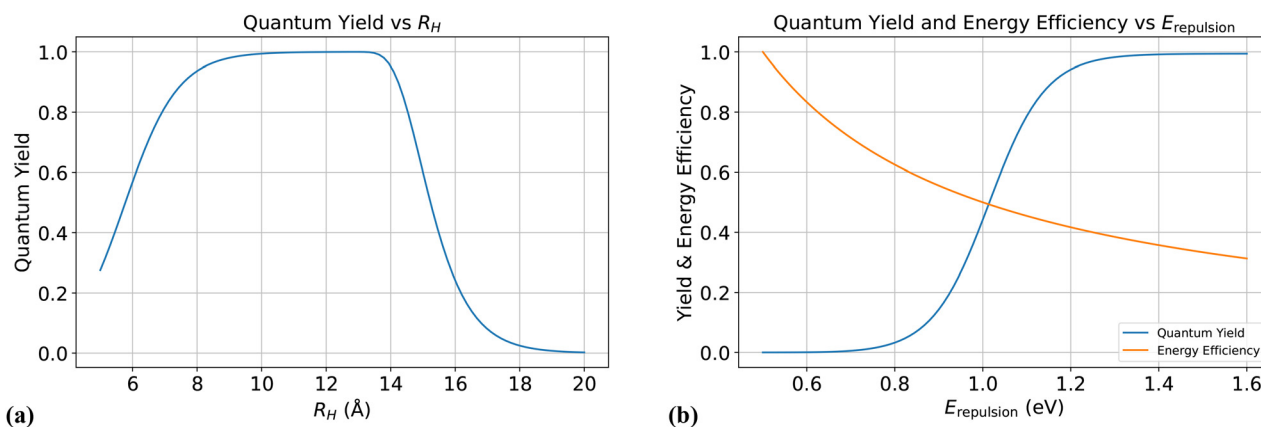


Fig. 5 Simulated quantum yield dependence on key HB network parameters. Both plots utilize representative constant values for several parameters, based on optimized or typical values from our previous work:¹⁰ $R_{\text{L}} = 5$ Å, inter-cofactor path distance = 5 Å, $\lambda = 1.0$ eV, $E_{\text{W}_2}^{(0)} = 1.1$ V, $E_{\text{P}_{\text{Min}}}^{(0)} = 1.6$ V (and other intermediate potentials as specified in the simulation code). For plot (a), repulsion is fixed at 1.6 eV; for plot (b), R_{H} is fixed at 10 Å. (a) Quantum yield initially increases as R_{H} increases from 5 Å. This improves the condition $R_{\text{H}} > R_{\text{L}}$, kinetically favoring the initial transfer of the higher-energy (hot) hole towards the hot pathway (W_{H_1}) over the cold pathway (W_{L_1}), thereby promoting successful bifurcation. The yield peaks within an optimal range (9–14 Å), consistent with the ‘sweet spot’ identified by SHAP analysis. As R_{H} increases further (> 14 Å), the yield drops significantly because the rate of the first crucial hole transfer step ($k_{\text{W}_1 \rightarrow \text{W}_{\text{H}_1}}$) decreases exponentially with distance due to the decay of the electronic coupling term (V_{ij}^2) in the MJL rate expression (eqn (1)), becoming too slow to compete effectively with potential recombination or undesired pathways within the simulation time. (b) Quantum yield shows a threshold dependence on the electrostatic repulsion energy. Below 0.8 eV, the yield is negligible, indicating insufficient driving force for efficient bifurcation. The yield rises sharply between 0.8 eV and 1.3 eV as repulsion provides the critical energy to drive the hot hole transfer, plateauing near unity for repulsion > 1.3 eV. Concurrently, the energy efficiency (orange curve), calculated *via* eqn (9), decreases monotonically with increasing repulsion. Plotting both metrics visually demonstrates the crucial design trade-off: maximizing yield requires high repulsion (> 1.3 eV), while maximizing energy efficiency favors low repulsion. The optimal range for both high quantum yield and acceptable energy efficiency, therefore, lies in a compromise region, consistent with the SHAP analysis sweet spot (1.25–1.71 eV), where yield is high but the energetic cost of repulsion is not excessive. (a) Quantum yield dependence on R_{H} . Besides R_{H} , which is varied from 5 Å to 20 Å, all other parameters are held constant at the representative values listed in the main caption. (b) Quantum yield and energy efficiency dependence on repulsion energy. Besides the repulsion energy, which is varied from 0.5 eV to 1.6 eV, all other parameters are held constant at the representative values listed in the main caption.



unit quantum yield can only be realized with an energy efficiency of 30–40%. If we require the design to realize very high energy efficiency, the quantum yield for EB would be very small.

The design examples in Fig. 5 underscore the non-linear relationships involved in designing high-performance HB networks, reinforcing the value of comprehensive statistical analysis and machine learning in network design.

3.4 Summary

Our analysis finds three key design principles that are required to realize efficient light-driven hole bifurcation in the design frameworks that we have explored. First, positioning the first hot-hole acceptor further from the bifurcation site than the first cold-hole pathway acceptor ($R_H > R_L$) consistently enhances the HB quantum yield. This relationship is supported robustly by both the Pearson correlation and SHAP-based feature importance analysis. Second, while increasing electrostatic repulsion between the two injected holes markedly increases the quantum yield (by providing the driving force needed to accelerate hole transfer), increasing this repulsion energy concomitantly lowers the HB energy efficiency. This finding highlights a central trade-off in the design of closed-system hole or electron transfer.²⁸ Third, our machine learning models pinpoint “sweet-spots” in design space for each critical network parameter, capturing the nonlinear influence of inter-cofactor distances, redox potentials, and electrostatic interactions on quantum yield performance, and thereby offering concrete targets for experimental realizations. Taken together, these findings show that integrating detailed kinetic modeling with statistical and machine learning can direct the design of optimal HB networks by directing us to regions of design space that are not obvious choices based on intuition grounded, largely, in our understanding of single-step redox processes.

4 Conclusion

We have explored and characterized the key determinants of efficient hole bifurcation networks. The designs emerged through integrated computational, statistical, and machine learning analysis. Our findings indicate that optimizing HB performance requires thoughtful design of both network geometry and energetics. Positioning the cofactor nearest to the bifurcating site on the hot-hole pathway at longer distances from the bifurcation site compared to that of the cold-hole counterpart ($R_H > R_L$) substantially increases the quantum yields, because the larger R_H value suppresses short-circuiting of the hot hole onto the cold pathway, enforcing preferential routing of each hole to its intended branch. Installing strong electrostatic repulsion between the two holes on the bifurcation site is crucial for realizing high quantum yields, but negatively impacts the network energy efficiency. We also identified key parameter “islands” that produce high quantum yields and acceptable energy efficiencies. Specific ranges for important parameters, such as R_H (11.24–14.5 Å) and electrostatic repulsion (1.25–1.71 eV) balance quantum yield (90% to 100%) and

energy efficiency (30% to 40%). Our findings underscore the promise of combining computational modeling with advanced statistical and machine learning methodologies to reveal design principles for electron and hole bifurcation networks.

The strategy that we described here (large-scale network enumeration → kinetic simulation → correlation/statistical screening → interpretable ML feature-analysis) constitutes a general design framework for engineered charge-transport networks. While our study focused on light-driven hole bifurcation in *de novo* proteins, the approach can be extended to design other complex multi-site networks. Networks of this kind might also be used for complex materials assembly or chemical catalysis, enabling the design of functional far-from-equilibrium systems.

Conflicts of interest

There are no conflicts to declare.

Data availability

All data that support the findings of this study are available in the manuscript and the supplementary information (SI). Supplementary information is available. See DOI: <https://doi.org/10.1039/d6cp00473c>.

Acknowledgements

This work was supported by the W. M. Keck Foundation and the National Science Foundation (CHE-2528383 and CHE-2528384). We also acknowledge support of the Duke University Shared Cluster Resource (DSCR).

References

- 1 J. W. Peters, *et al.*, A new era for electron bifurcation, *Curr. Opin. Chem. Biol.*, 2018, **47**, 32–38.
- 2 W. Buckel and R. K. Thauer, Flavin-based electron bifurcation, a new mechanism of biological energy coupling, *Chem. Rev.*, 2018, **118**, 3862–3886.
- 3 J. L. Yuly, C. E. Lubner, P. Zhang, D. N. Beratan and J. W. Peters, Electron bifurcation: progress and grand challenges, *Chem. Commun.*, 2019, **55**, 11823–11832.
- 4 J. L. Yuly, P. Zhang and D. N. Beratan, Energy transduction by reversible electron bifurcation, *Curr. Opin. Electrochem.*, 2021, **29**, 100767.
- 5 N. F. Polizzi and W. F. DeGrado, A defined structural unit enables *de novo* design of small-molecule-binding proteins, *Science*, 2020, **369**, 1227–1233.
- 6 N. F. Polizzi, Y. Wu, T. Lemmin, A. M. Maxwell, S.-Q. Zhang, J. Rawson, D. N. Beratan, M. J. Therien and W. F. DeGrado, *De novo* design of a hyperstable non-natural protein-ligand complex with sub-Å accuracy, *Nat. Chem.*, 2017, **9**, 1157–1164.



- 7 S. I. Mann, A. Nayak, G. T. Gassner, M. J. Therien and W. F. DeGrado, De novo design, solution characterization, and crystallographic structure of an abiological Mn-porphyrin-binding protein capable of stabilizing a Mn (V) species, *J. Am. Chem. Soc.*, 2020, **143**, 252–259.
- 8 L. Lu, X. Gou, S. K. Tan, S. I. Mann, H. Yang, X. Zhong, D. Gazgalis, J. Valdiviezo, H. Jo, Y. Wu, M. E. Diolaiti, A. Ashworth, N. F. Polizzi and W. F. DeGrado, De novo design of drug-binding proteins with predictable binding energy and specificity, *Science*, 2024, **384**, 106–112.
- 9 J. L. Yuly, P. Zhang, C. E. Lubner, J. W. Peters and D. N. Beratan, Universal free-energy landscape produces efficient and reversible electron bifurcation, *Proc. Natl. Acad. Sci. U. S. A.*, 2020, **117**, 21045–21051.
- 10 X. Huang, J. Yuly, P. Zhang, W. DeGrado, M. Therien and D. Beratan, Design of light driven hole bifurcating proteins, *ACS Cent. Sci.*, 2025, **11**, 1911–1920.
- 11 C. E. Lubner, *et al.*, Mechanistic insights into energy conservation by flavin-based electron bifurcation, *Nat. Chem. Biol.*, 2017, **13**, 655–659.
- 12 J. L. Yuly, P. Zhang, X. Ru, K. Terai, N. Singh and D. N. Beratan, Efficient and reversible electron bifurcation with either normal or inverted potentials at the bifurcating cofactor, *Chem*, 2021, **7**, 1870–1886.
- 13 K. Terai, J. L. Yuly, P. Zhang and D. N. Beratan, Correlated particle transport enables biological free energy transduction, *Biophys. J.*, 2023, **122**, 1762–1771.
- 14 H. B. Gray and J. R. Winkler, Electron tunneling through proteins, *Q. Rev. Biophys.*, 2003, **36**, 341–372.
- 15 V. G. Levich and R. R. Dogonadze, Theory of nonradiative electron transitions between ions in solution, *Dokl. Akad. Nauk SSSR*, 1959, **124**, 123–126.
- 16 J. Jortner, Temperature dependent activation energy for electron transfer between biological molecules, *J. Chem. Phys.*, 1976, **64**, 4860–4867.
- 17 J. J. Hopfield, Electron transfer between biological molecules by thermally activated tunneling, *Proc. Natl. Acad. Sci. U. S. A.*, 1974, **71**, 3640–3644.
- 18 C. E. Wise, A. E. Ledinina, D. W. Mulder, K. J. Chou, J. W. Peters, P. W. King and C. E. Lubner, An uncharacteristically low-potential flavin governs the energy landscape of electron bifurcation, *Proc. Natl. Acad. Sci. U. S. A.*, 2022, **119**, e2117882119.
- 19 H. Kless and W. Vermaas, Combinatorial mutagenesis and structural simulations in the environment of the redox-active tyrosine Y_Z of photosystem II, *Biochemistry*, 1996, **35**, 16458–16464.
- 20 A.-M. A. Hays, I. R. Vassiliev, J. H. Golbeck and R. J. Debus, Role of D1-His190 in the proton-coupled oxidation of tyrosine YZ in manganese-depleted photosystem II, *Biochemistry*, 1999, **38**, 11851–11865.
- 21 S. Styring, J. Sjöholm and F. Mamedov, Two tyrosines that changed the world: Interfacing the oxidizing power of photochemistry to water splitting in photosystem II, *Biochim. Biophys. Acta, Bioenerg.*, 2012, **1817**, 76–87.
- 22 T. J. Meyer, M. H. V. Huynh and H. H. Thorp, The possible role of proton-coupled electron transfer (PCET) in water oxidation by photosystem II, *Angew. Chem., Int. Ed.*, 2007, **46**, 5284–5304.
- 23 S. J. Mora, E. Odella, G. F. Moore, D. Gust, T. A. Moore and A. L. Moore, Proton-coupled electron transfer in artificial photosynthetic systems, *Acc. Chem. Res.*, 2018, **51**, 445–453.
- 24 G. James; D. Witten; T. Hastie and R. Tibshirani, *An introduction to statistical learning: with applications in R*, Springer, 2013, vol. 103.
- 25 T. Chen and C. Guestrin, XGBoost: A scalable tree boosting system, Proceedings of the 22nd ACM SIGKDD International Conference on Knowledge Discovery and Data Mining, 2016, pp. 785–794.
- 26 C. Goutte and E. Gaussier, A probabilistic interpretation of precision, recall and F-score, with implication for evaluation, European conference on information retrieval, 2005, pp. 345–359.
- 27 S. M. Lundberg and S.-I. Lee, A unified approach to interpreting model predictions, *NIPS'17: Proceedings of the 31st International Conference on Neural Information Processing Systems*, 2017, pp. 4768–4777.
- 28 J. D. Schultz, K. A. Parker, M. J. Therien and D. N. Beratan, Efficiency limits of energy conversion by light-Driven redox chains, *J. Am. Chem. Soc.*, 2024, **146**, 32805–32815.

